

Semi-free oscillation method for dynamic stability characterization on re-usable launcher first-stage

S. Paris and A. Viladegut***

**von Karman Institute for Fluid Dynamics
sebastien.paris@vki.ac.be*

***von Karman Institute for Fluid Dynamics
alan.viladegut@vki.ac.be*

Abstract

Interest in new strategies for launch services dedicated to micro-satellites is growing. In the framework of the development of new launch solutions based on re-usable first stages, VKI focus on the dynamic stability of the launcher in transonic and supersonic regime.

The development of a new semi-free oscillations method to measure the damping parameter of slender body is presented. The design process of the system is described. The similitude rules and the processing method used in this project are explained. Static pitching moment coefficients and associated damping coefficients are measured in transonic and supersonic regime. The outcomes of the test campaign shows that results are repeatable and within acceptable uncertainty margins.

1 Introduction

Interest in new strategies for launch services dedicated to micro-satellites (<250 kg) is growing over the world. The development of new launch solutions based on re-usable first stages is paving the way to a more flexible, costly efficient and environmentally friendlier strategy that satisfies the needs of small satellite market. In this framework, the Recovery and Return-to-Base (RRTB) project [9] is conceived by a consortium of leading European companies and institutions to explore a novel technology aiming at recovering the first stage of the MESO launcher.

As one of the partners within this consortium, the von Karman Institute (VKI) contributes to the generation and validation of an aerodynamic database using wind tunnel experiment. The vehicle's stability in transonic and supersonic is critical for the trajectory estimation [10]. The development of a new semi-free oscillations method to measure the damping parameter of the system is presented. The method is based on the work of Kovacs et al. [11], in which a system of springs and cables were attached to a slender body and routed outside the test chamber to characterize the dynamic response of the system. The present work focus on the minimization of the interactions between the supporting devices and the air flow by using internal springs. The dynamic response of the system is captured with a high-frequency magnetic encoder, which ease the data processing and provides better accuracy than the high-speed cameras used in the past.

The design and manufacturing process of the system is described. The similitude rules and the processing method used in this project are explained. A parametric study using springs with different stiffness gives the sensitivity to the natural frequency of the launcher. Static pitching moment coefficients and associated damping coefficients are measured in transonic and supersonic regime. The outcomes of the test campaign shows that results are repeatable and within acceptable uncertainty margins.

Only the subsonic results are display in this paper, but the same activity was carried out at Mach 2.0. It is why the model, the balance and the equipment were designed taking into account this case.

2 Reference data and facility description

2.1 Reference geometry

The reference geometry of the MESO launcher's first stage was supplied by Pangea Aerospace. Reference dimensions are taken from [1] and [3], and they are shown in Figure 1. The length of the vehicle from nose to the base is 13.1802 m, but the reference length (L_{ref}) considered for aerodynamic coefficients is 14.5122 m. The reference surface for aerodynamic coefficients (S_{ref}) corresponds to the area of a circle with 1.5 m in diameter, leading to an S_{ref} of 1.767145 m². The Center of Gravity (CoG) is located at 6.8362 m from the nose tip, and it passes through the longitudinal axis of the vehicle.

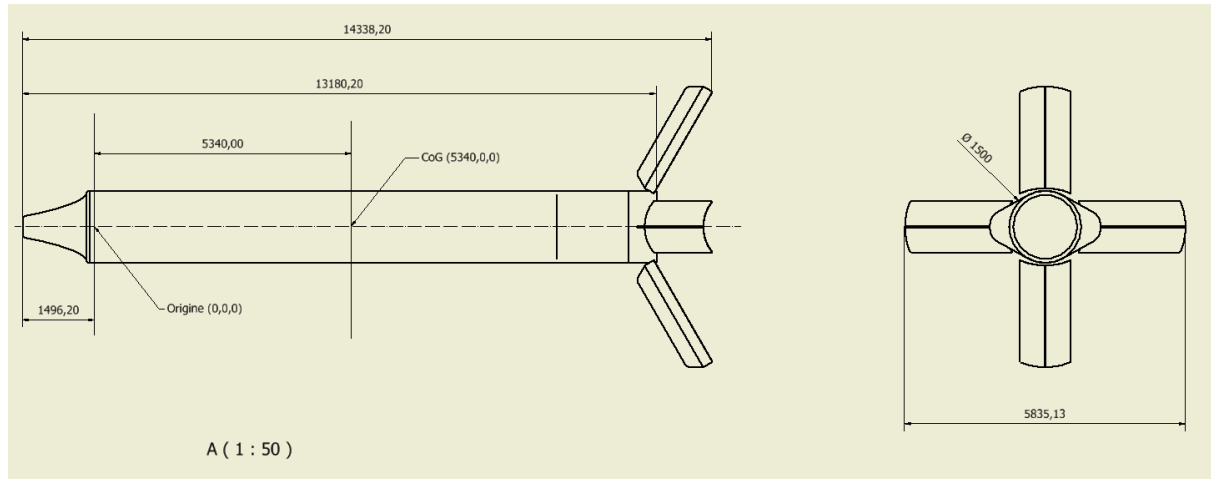


Figure 1. Reference geometry at scale 1:1

2.2 Reference AEDB

In order to design the model and the balance for wind tunnel testing, we should estimate the aerodynamic efforts at which the system will be subject to. Preliminary aerodynamic coefficients were provided by CFD computations performed by Deimos Space [7]. The results of those simulations are considered as a reference Aerodynamic Database (AEDB) for this activity. The Table 1 summarizes the reference aerodynamic coefficient extracted from these plots at 5° and 10° of Angle of Attack (AoA). These values will be used to estimate the forces acting on the wind tunnel model and they will contribute to the balance design.

| Mach | AoA | C_D | C_L | C_m | AoA | C_D | C_L | C_m |
|------|-----|-------|-------|-------|-----|-------|-------|-------|
| 0.7 | 5 | 8 | 0.5 | 0.3 | 10 | 8 | 0.8 | 0.4 |
| 0.9 | 5 | 9 | 0.3 | 0.15 | 10 | 9 | 0.5 | 0.25 |
| 2 | 5 | 7 | 0.5 | 0.15 | 10 | 7.5 | 1.5 | 0.4 |
| 6 | 5 | 4 | 1 | 0.35 | 10 | 6 | 1.8 | 0.8 |

Table 1: Reference aerodynamic coefficients at 5° and 10° AoA.

2.3 Transonic and supersonic wind tunnel (S1)

The VKI supersonic/transonic wind tunnel S-1 is a continuous closed-circuit facility of the Ackeret type, driven by a 615 kW axial flow compressor. A sketch of the facility is shown in Figure 2. Two test sections are available depending on the flow requirements: supersonic or transonic. In the former, the contoured nozzle ends in a section 0.4 by 0.4 m, and it is designed specifically for testing at Mach 2.0. In the latter, a slotted transonic section measures 0.4 m by 0.36 m and it offers variable Mach number capabilities depending on the power used to drive the compressor, from 0.3 to 1.05. A typical unit Reynolds number is 4·10⁶/m. The test section contains a three-degree-of-freedom traversing

mechanism for model and/or probe support, as well as a variable incidence angle mechanism that ranges between $\pm 35^\circ$. For the test campaign reported below, only the transonic section is used.

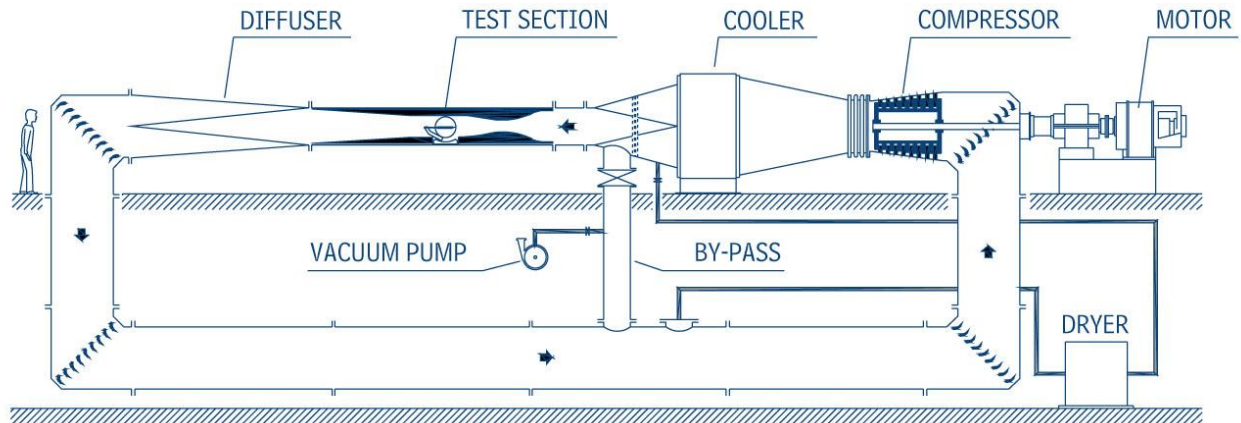


Figure 2: S1 Wind tunnel

Flow conditions of the experimental tests are summarized in the following table:

| Mach | P_0 [Pa] | P_∞ [Pa] | Re/L_{ref} [10^6] | T_0 [K] | ρ_∞ [kg/m^3] | U_∞ [m/s] |
|------|------------|-----------------|-------------------------|-----------|-----------------------------------|------------------|
| 0.7 | 26666 | 19224 | 0.8993 | 313 | 0.2350 | 236.91 |
| 0.8 | 26666 | 17494 | 0.9386 | 321 | 0.2142 | 270.50 |
| 0.9 | 26666 | 15767 | 0.9567 | 329 | 0.1940 | 303.55 |
| 2 | 10000 | 1278 | 0.3187 | 329 | 0.0249 | 537.04 |

Table 2: Typical test conditions for the different Mach numbers ($L_{ref}=0.2902\text{m}$).

3 Static stability in transonic

Static tests will be performed in transonic regime in the S1 wind tunnel. The purpose is to measure the aerodynamic forces and moments acting on the model inserted in the air flow. The model is equipped with a 3 components balance, which leads to the measurement of 2 forces (axial and normal to the flow) and 1 moment for each test run. The design process of test models and balances are described below, together with their calibrations.

3.1 Model design for transonic and supersonic test

3.1.1 Definition of the scale

The limitation in S1 wind tunnel is the blockage effect. The model must be big enough to contain the equipment, but small enough to minimize flow perturbations due to the limited space in the test section. The typical blockage ratio accepted in S1 under transonic regimes is 3%. The value can be so high because of the slotted walls conforming the test chamber, which allow the flow to pass through in the presence of normal pressure gradients.

The blockage effect has been assessed for S1 using different model scales and positions. Details of blockage and dimensions are given in Table 3 based on the reference model seen in Figure 1. The scale 1/50 is selected for the limited blockage and because the model can fit better for visual access through the side windows.

| Scale | 1/1 | 1/45 | 1/50 |
|------------------------|---------|----------|----------|
| Length[m] | 13.1802 | 0.292893 | 0.263604 |
| Diam. [m] | 1.5 | 0.03333 | 0.03 |
| D Decel.[m] | 5.83513 | 0.12967 | 0.03 |
| AoA=0° | | | |
| Area [m ²] | 11.2 | 0.005531 | 0.00448 |
| Blockage[%] | | 3.457 | 2.8 |
| AoA=10° | | | |
| Area [m ²] | 13.32 | 0.006579 | 0.00448 |
| Blockage [%] | | 3.45679 | 3.33 |

Table 3: Selection of the scale

3.1.2 Design solution and manufacturing

The model has been manufactured in ABS by 3D printing technique. This an efficient cost-effective solution for components with complex geometries. The material presents plastic deformation well above the maximum temperatures expected in the tunnel, and aerodynamic loads are not high enough as to produce elastic deformation during a test run.

The design solution adopted for the system consists of 3 main components: i) the external shell of the model, ii) the nose cap, iii) the balance. These elements are shown in Figure 3. The external shell corresponds to the lateral walls of the vehicle and the drag device, and it encapsulates the instrumented balance. The connection between the external shell and the balance is achieved with a squared interface close to the nose tip, which will prevent the shell from turning around the longitudinal axis, and it transmits the aerodynamic loads from the body to the balance. A nut screwed on the balance fixes the two elements longitudinally. Then, the nose tip, also manufactured in ABS, is fixed into the external shell to close the model.

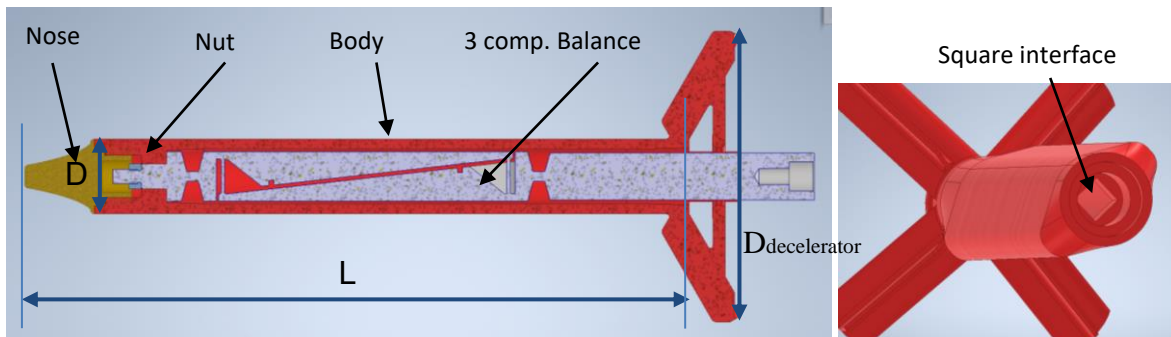


Figure 3. Static model integration for S-1 tests.

Note, however, that the reference geometry cannot be fully respected due to structural limitations. The main differences are shown in Figure 4. First, the four flaps are prolonged and fixed up to the body surface, which was not the case in the reference geometry. Then, some elements around the drag device were too thin to be scaled properly. Therefore, thicknesses of fins and flaps are increased so that they can be manufactured properly and sustain aerodynamic loads without reaching the elastic limit. Care is taken not to increase the area of the surface normal to the flow in the process, so that flight similarity issues are avoided, and aerodynamic coefficients remain relevant. Moreover, a rounded corner is added on the rear of the flap, at the hinge with the main body, to prevent potential flexion during the test. Finally, a new structure was added downstream of the drag device to increase the rigidity of the whole system. This structural element is assumed to have a negligible effect on the aerodynamic coefficients because it is placed in a region where the flow is already detached from the body.

FEM tools were used to confirm the stiffness of this structure under maximum load. The maximum C_p distribution computed by Deimos was used to estimate the load on a flap. This load was applied to the four flaps. A very conservative approach gives 30N per flap. The resulting stress distribution never exceeded 5 MPa, which is well below the elastic limit of ABS.

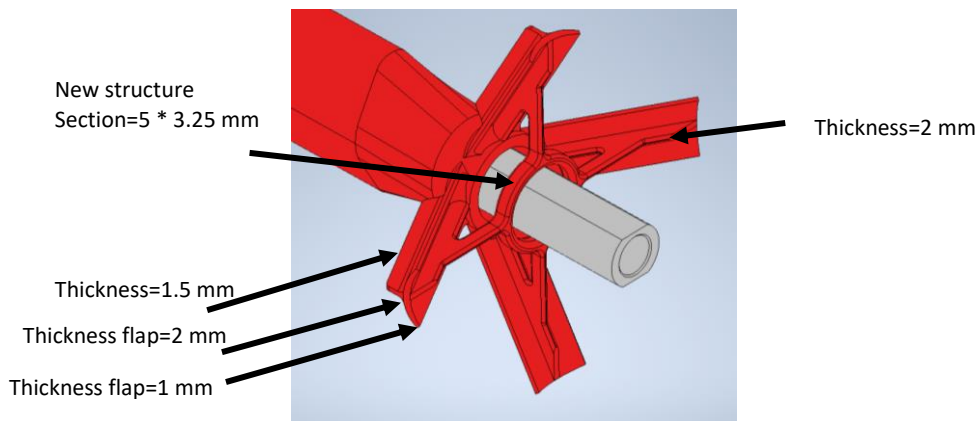


Figure 4: Modification of the thickness

3.2 Balance design for transonic and supersonic test in S1

The forces and moments acting on the model are estimated using the aerodynamic coefficients obtained by CFD provided in Table 1 and the S1 test conditions given in Table 2. Results are gathered in Table 4 for different combinations of Mach number and AoA of the model. A safety factor of 1.5 is applied to the highest values, and the final working range of the balance is given in Table 5. As the lift was very small compared to drag, its range was increased to 10 N.

| Mach | Model @ 5° | | | Model @ 10° | | |
|------|------------|---------|------------|-------------|---------|------------|
| | D [N] | L [N] | M_y [Nm] | D [N] | L [N] | M_y [Nm] |
| 0.7 | 37.32 | 2.33 | 0.406 | 37.32 | 3.73 | 0.541 |
| 0.9 | 57.26 | 1.91 | 0.277 | 57.26 | 3.18 | 0.461 |
| 2.0 | 16.82 | 1.20 | 0.105 | 18.02 | 3.60 | 0.279 |

Table 4: Estimation of forces and moments acting on the model in S1.

| D [N] | L [N] | M_y [Nm] |
|---------|---------|------------|
| 85 | 10 | 0.8 |

Table 5: Range of the balance for S1 tests.



Figure 5: Balance for transonic / supersonic activities

3.2.1 Calibration of the balance

A special interface was designed and built for the calibration of the balance (see Figure 6). It allows to apply pure forces and moment at the centre of the balance. The balance and this interface were installed horizontally on the calibration bench. Forces are applied through calibrated set of mass and pulley. The alignment of the forces with the

balance is made using a self-leveling laser. During the calibration process, the output voltage from the strain gages is measured for each known load being applied on the balance.

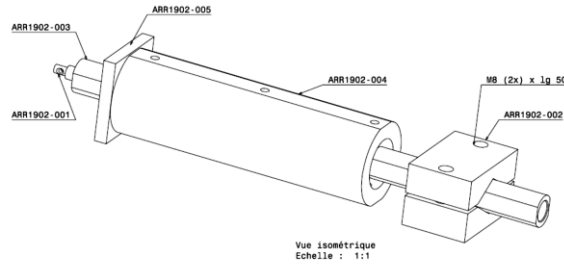


Figure 6: Interface for the calibration

The calibration matrix M , which relates forces and voltages through $[U] = [M][F]$, with F and U being the vectors of applied loads and output voltages, respectively, is deduced from these measurements. Then, the inverted matrix M^{-1} allows to obtain the load from the measured voltage during the test, with $[F] = [M^{-1}].[U]$. Matrices M and M^{-1} are given below. It is observed that interferences between the components are very small (diagonal components are much bigger than other terms).

$$M = \begin{pmatrix} -0.0089058 & 0.00010377 & 0.002992 \\ -0.000136 & 0.0589575 & -0.0055577 \\ -4.037 \times 10^{-5} & 0.00058204 & -0.8418944 \end{pmatrix}$$

$$M^{-1} = \begin{pmatrix} -112.28755 & 0.20159265 & -0.4003863 \\ -0.2584745 & 16.9629393 & -0.1128989 \\ 0.00520517 & 0.01171758 & -1.1878563 \end{pmatrix}$$

3.3 Results of static stability in transonic

Before starting the test campaign, the model is installed inside the chamber of the wind tunnel. The model is mounted on a horizontal sting that can move vertically using two motors. Different displacements at two different points of this axis allows the rotation of the model with respect to the flow inside the wind tunnel. The angle of attack is calibrated with the position of these motors before the wind tunnel campaign.

The procedure followed to measure the static stability coefficients is rather simple. The model is installed at 0° before starting the facility. Then, the static pressure in the wind tunnel is reduced and the engine is run to increase the total pressure up to 26666 Pa. The Mach number and the total pressure are measured using static and Pitot probes connected to pressure transducers.

Once the flow is set at requested Mach number, and starting with the model positioned at 0° , the output from the balance is recorded into the computer. Then, without stopping the flow, the model is positioned at another angle of attack using the 2 motors mentioned before. The AoA is changed every 0.5° up to $+8^\circ$, then the model is moved back to 0° and the range down to -8° is covered. A last measurement at 0° is finally made. Sweeping the angle of attack between -8 and $+8^\circ$ allows measuring the axial (F_x) and normal forces (F_z), as well as the pitching moment (M_y), at different conditions. The dynamic pressure in the wind tunnel and the reference surface of the model are used to convert these forces and moment into adimensional coefficients: CF_x , CF_z and CM_y . A rotation matrix is used to compute the lift and drag coefficients from CF_x , CF_z .

The measured values of CF_x and C_D are plotted in Figure 7. Two repeatability tests were performed. Both CF_x and C_D present a low dependence on the angle of attack, as was already observed in inviscid simulations performed by Deimos [3]. Values oscillate between 6 and 6.8, which is lower than the value predicted by the simulations, but all measurements remain well above the required minimum drag performance, hence validating the design proposed for the re-entry vehicle.

The normal and lift coefficients are provided in Figure 8. A linear trend is observed in CF_z and it is independent of the Mach number.

The lift coefficient has also a linear trend. The effect of the normal force is too small to be visible on this plot. The values are always higher than the prediction given by the inviscid simulation and the lift coefficient remains independent of the Mach number.

The pitching moment coefficients are shown in Figure 9. Their trend is fairly linear, and the slope is always negative, indicating that the system is statically stable. Measured values are clearly higher than those predicted by Deimos using

CFD, producing a better stability in this regime (higher slope). The slopes of C_m at trim angle are presented in Table 6. These values will be used later for the calculation of the target frequency.

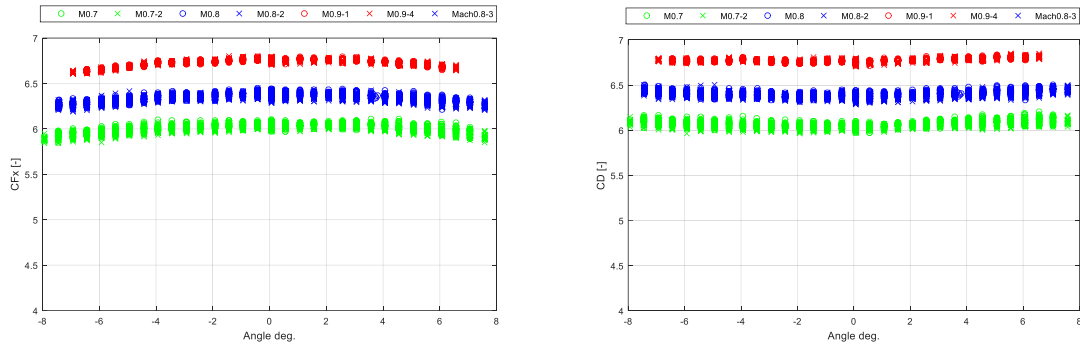


Figure 7: Measured axial and drag coefficients for longitudinal stability

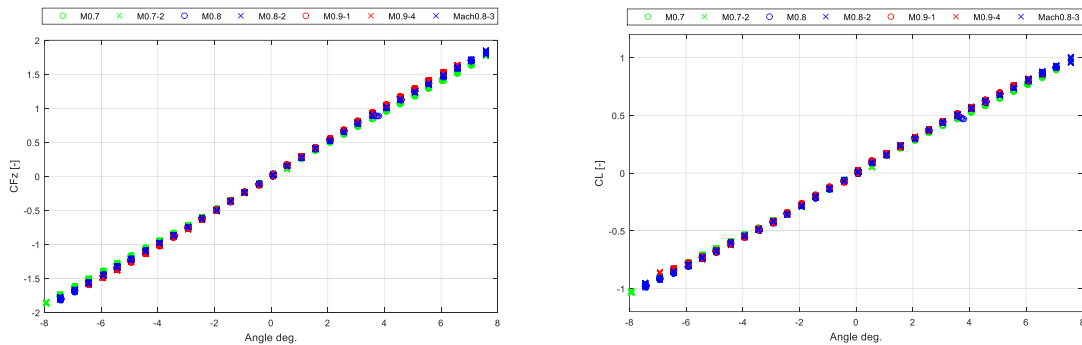


Figure 8: Measured normal and lift coefficients for longitudinal stability

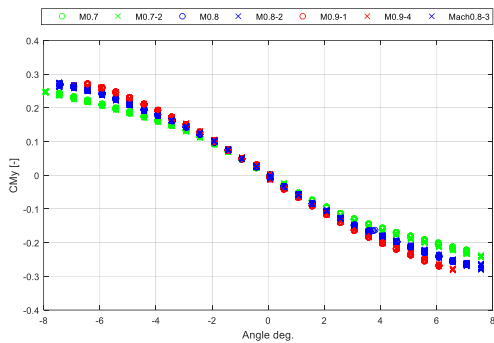


Figure 9: Measured moment coefficient for longitudinal stability

| Mach | $C_{m\theta}$ [rad^{-1}] |
|------|------------------------------|
| 0.7 | -2.82 |
| 0.8 | -3.02 |
| 0.9 | -3.21 |

Table 6: Slope of the pitching moment

4 Dynamic stability in transonic

The purpose of the dynamic tests is to measure the damping parameter of the MESO launcher in transonic conditions. An innovative semi-free oscillation methodology has been developed to characterize the dynamic response of the vehicle. The logic of the concept is to position the model off the trim angle at the initial state, release the system and bring it back to equilibrium with the help of an internal spring. In the process to reach equilibrium, the model oscillates at specific frequencies for a short period of time. These frequencies are representative of the flight condition. Then,

dynamic stability coefficients of the vehicle can be deduced from the time-resolved attitude of the model being measured with a fast response magnetic encoder.

In the following, the design process of the test setup is described, and the results of the wind tunnel test campaign in S1 under subsonic conditions are provided.

4.1 Similitude with flight

To design the dynamic test setup, the equation describing the movement of the vehicle (and the model) is considered. The governing equation of a body oscillating around its center of gravity is [4]:

$$I_{yy}\ddot{\theta} - (Cm_q + Cm_{\dot{\alpha}})\frac{q_{\infty}S_{ref}L_{ref}^2}{2U_{\infty}}\dot{\theta} - q_{\infty}S_{ref}L_{ref}Cm_{\theta}\theta - k\theta = 0 \quad (1)$$

with:

| | |
|----------------------------|---|
| θ | pitch angle |
| I_{yy} | moment of inertia |
| q_{∞} | Dynamic pressure |
| S_{ref} | Reference surface |
| L_{ref} | Reference length |
| U_{∞} | Speed |
| Cm_{θ} | Slope of the pitching moment versus angle of attack |
| $Cm_q + Cm_{\dot{\alpha}}$ | derivative in pitch (damping parameter) |

The longitudinal attitude of the vehicle is fully characterized through the aerodynamic coefficients Cm_{θ} and $Cm_q + Cm_{\dot{\alpha}}$. The former defines the static stability of the system, and it is quantified through the previous static stability campaign in S1, as described in Section 3; whereas the latter is the damping parameter of the dynamic system, and it is the target quantity to be measured in the test campaign that follows.

To obtain similarity with flight, the semi-free oscillation method requires the system on ground to oscillate at very specific frequencies. The definition of these frequencies relies on the Strouhal number, which is normally used to characterize the vortex shedding phenomena in the wake of a vehicle, and it can be understood here as a normalized frequency. The Strouhal number is defined as:

$$St = \frac{fD}{U_{\infty}} \quad (2)$$

where f is the frequency of the system and D is the diameter of the body. Then, the Strouhal similarity results in the following equality:

$$St_{EXP} = St_{FLIGHT} = \frac{1}{2\pi} \sqrt{\frac{q_{\infty}S_{ref}D^3Cm_{\theta}}{I_{yy}U_{\infty}^2}} \Big|_{FLIGHT} \quad (3)$$

leading to:

$$f_{EXP} = \frac{1}{2\pi} \sqrt{\frac{q_{\infty}S_{ref}D^3Cm_{\theta}}{I_{yy}U_{\infty}^2}} \Big|_{FLIGHT} \frac{U_{\infty}}{D} \Big|_{EXP} \quad (4)$$

Considering a reference inertia I_{yy} in the flight of 47777 kgm² [7], and using the flight conditions from the preliminary CFD database, the oscillation frequencies of the experimental setup can be estimated before the static stability campaign for design purposes. Values reported in Table 7 are obtained using aerodynamic coefficient Cm_{θ} measured in the wind tunnel. A 5th order polynomial fitting is generated using Cm_y measurements against θ , and the slope is extracted at trim angle. A slope is found with this procedure, which according to Eq. 4, leads to a target f_{exp} . It shows that maximum target frequencies in the test are around 32 Hz for Mach 2.0. This condition is not shown in this paper, but the model and the spring must be able to reach this frequency. That means the model must be very light and the spring very stiff.

| Mach | U_∞ [m/s] | ρ_∞ [kg/m ³] | Cm_θ [rad ⁻¹] | $U_{\infty,S1}$ [m/s] | f_{EXP} [Hz] |
|------|------------------|------------------------------------|----------------------------------|-----------------------|----------------|
| 0.7 | 204.2 | 0.164 | -2.82 | 243 | 20.2 |
| 0.8 | 233.4 | 0.148 | -4.52 | 278 | 22.5 |
| 0.87 | 253.8 | 0.14 | -4.58 | 302 | 18.8 |
| 2.0 | 590.08 | 0.0925 | -2.7 | 515 | 32 |

Table 7: Frequency f_{exp} of the dynamic system based on static tests

4.2 Mechanical solution for dynamic test

The dynamic test setup design requirements of the dynamic test setup should consider: i) a fixed support system to place the model inside the chamber of the wind tunnel; ii) an interface that allows the model to oscillate around a fixed reference point; iii) a spring to bring the model to equilibrium position; iv) an actuator that positions the model off equilibrium at the initial state of the recording.

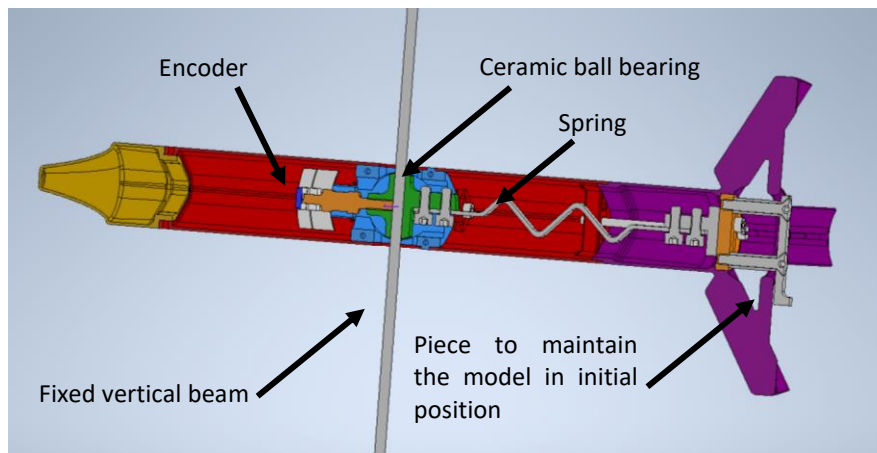


Figure 10: Mechanical design of dynamic model for S1

The proposed solution is shown in Figure 10. The spring element is considered internal to minimize aerodynamic interactions with the external flow. The model is supported by one single cable passing through the CoG, which goes from top to bottom of the test chamber. At the CoG, a cross-shaped static interface (green) is tightly fixed onto the cable to keep the model in place. Static elements, such as one of the tips of the spring or the sensing element included in the fast-response magnetic encoder that measures the angle of attack evolution in real time, are fixed to the static interface. Then, a dynamic interface (blue) can oscillate around the CoG through a system of ceramic ball bearings. This dynamic interface acts as a support for the external shell of the model (red), and for the magnetic plate that moves relative to the sensing element of the encoder is mounted on this shell. A sketch of both static and dynamic interfaces is shown in Figure 11. The nose (orange) and rear (purple) parts of the model are conceived modular to ease the system assembly, and they are pinned to the main frame before testing. The moving tip of the spring element is connected to the drag device. Finally, an L-shape piece is screwed onto the rear part of the drag device to connect the system with an external actuator that allows positioning the model off-equilibrium and release it at the initial condition.

The nose cap, the main body frame, the drag device, and the dynamic interface are manufactured in ABS through 3D printing. The internal springs and the static interface are made of steel. The fixations of the spring to the rear part of the body and other elements that are connected to the drag device are in Aluminium. All the screws are made of Titanium.

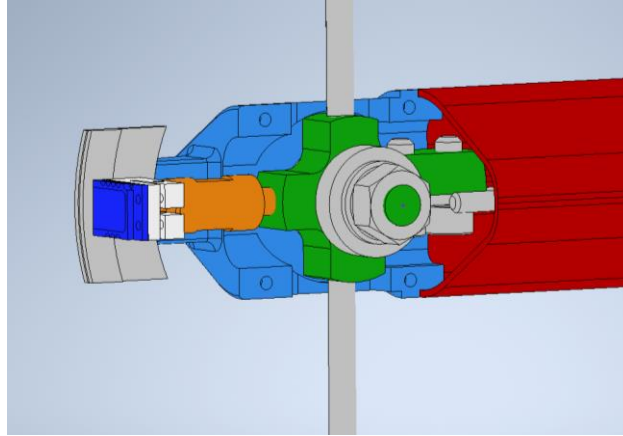


Figure 11: Detailed view of the oscillating system

4.2.1 Definition of the spring element

The oscillating frequency reached during the test (f_{exp}), the stiffness of the spring (k) and the inertia of the model (I_{yy}) are related through:

$$k = I_{yy}(2\pi f_{exp})^2 \quad (5)$$

The inertia of the dynamic model described above is 1040.21 kgmm² (from CAD). This leads to a spring with a stiffness of 42.84 Nm/rad if tested at 32.3 Hz, which is the highest f_{exp} estimated from CFD results as shown in Table 7.

Using such spring, the force needed to displace the model 10° from the trim angle is 52 N (static). During the oscillations, however, the spring could apply up to ±66 N (dynamic). These loads have been used to design the dynamic model. Furthermore, static and dynamic loads at each section of the model have been computed using FEM analysis, showing that the expected deformations were within the elastic limit.

The design of the spring is also important because it is not attached to the center of rotation. This means that, during oscillations, the spring must be able to bend and elongate. A simple blade could not be appropriate due to its high stiffness in traction. This is the reason why a w-shaped spring as that seen in

Figure 12 seem the most suitable solution.

Five springs with different thicknesses were selected as potential candidates to cover the full range of estimated f_{exp} . One should note, however, that the spring configuration during the test will be adapted at each Mach number according to f_{exp} based on Cm_α obtained during the static campaign. Since a perfect match between the required f_{exp} and the springs available remains difficult, we expect to test at 2 frequencies around the target one.

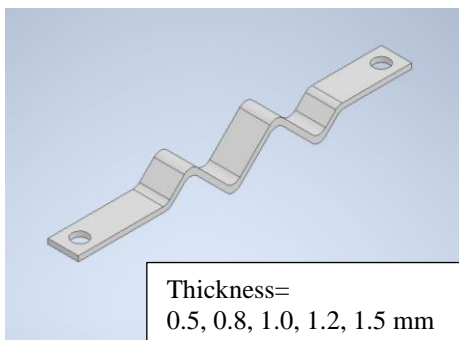


Figure 12: Spring element



Figure 13 : Magnetic encode

4.2.2 Encoder

A magnetic encoder from Renishaw (RLC2HDAD20K00C00 coupled with the ring MR080) was selected for its high accuracy and the absence of friction. The device is shown in Figure 13. It produces 350 counts per degree. The resolution is 0.0028 degrees for a maximum speed of 7.5 m/s. In our experiments the linear speed will not exceed 0.8 m/s with the model oscillating at 32 Hz.

4.2.3 Actuators

The dynamic system should be naturally stable thanks to the decelerator and the spring. This means that the oscillations of the model will be damped when going from an initial position off the trim angle towards its neutral position. Two pistons allow setting the model at the initial position, as shown in Figure 14.

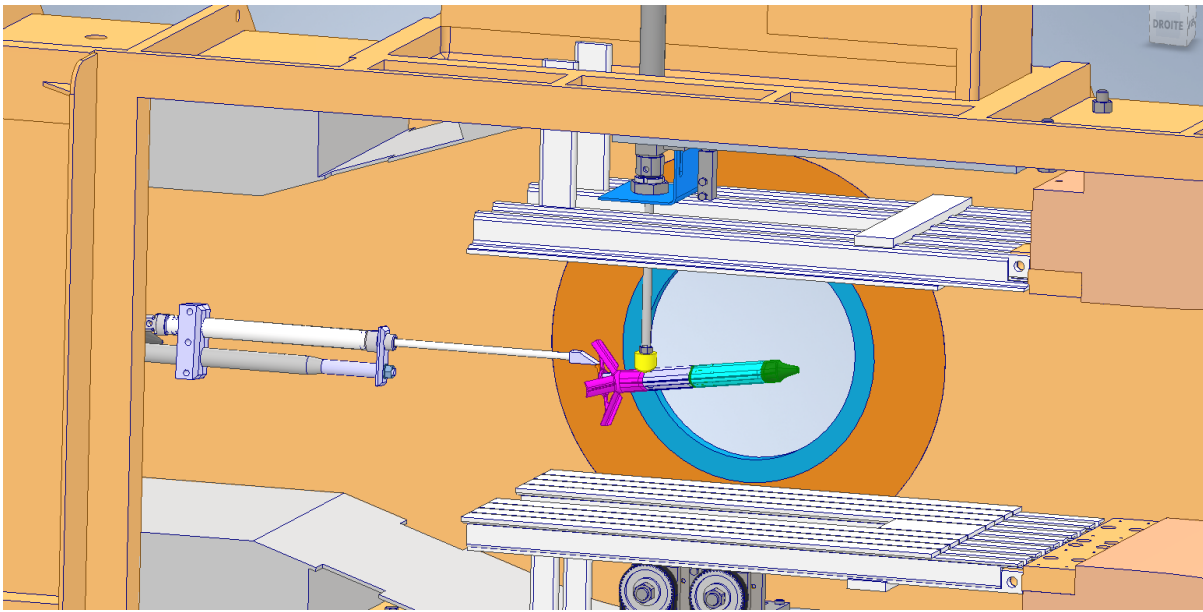


Figure 14: Actuators

The first piston is installed vertically above the model. It enters in contact with the model at the junction between the drag device and the main frame. The vertical position of the piston is set such that the initial angle of attack of the model is 10° . Unfortunately, the displacement of this piston is not fast enough when stiff springs are used, like that needed at 32 Hz. Therefore, a second piston is required to fix the model in position while the first one is retracted outside the test section.

The second piston is mounted horizontally behind the model. The model is released at t_0 with the retraction of the second piston.

For safety, the 2 pistons are controlled by 12 V electrovalve equipped with a special electronic device that allows a good synchronization between both pistons.

4.3 Test procedure

The duplication of the Strouhal number between flight and ground requires the definition of an oscillating frequency of the dynamic system that is proportional to $\sqrt{Cm_\theta}$, as seen in Eq. 4.

On the other hand, and based on Eq. 1, the stiffness of the dynamic system is a combination of an aerodynamic component that is proportional to Cm_θ (aerodynamic stiffness), and of a mechanical component k that depends on the spring's constant (mechanical stiffness). Therefore, the stiffness of the system will differ with and without flow.

For the dynamic tests, only the Cm_θ is needed to compute f_{exp} . The small differences observed on axial and normal coefficients are not present in the pitching moment coefficient, as shown in Figure 9.

When the springs are mounted inside the model, the stiffness (k) of the dynamic system must be measured. For that, known moments are applied on the model and the deflection angle is measured. Then, with the model installed in the test chamber and before running the tunnel, a series of tests are performed without flow to determine the frequency

and the inertia of the system in the vacuum through Eq. 5. To perform them, the model is deflected 6° from the steady state position using the 2 actuators described in Section 4.2.3. Once the system is released, the model goes back to equilibrium following an oscillation whose amplitude is damped in time. The fast-response encoder tracks the time-evolution of the angle of attack, and data are recorded into the system. From these measurements, both the frequency and the mechanical damping can be derived without the influence of aerodynamic forces.

Then, the wind tunnel is set at the requested Mach and the procedure just described is repeated. The angle of attack is recorded for more than 10 s. During the tests with flow, the frequency is slightly higher than that measured without flow because of the aerodynamic stiffness added to the system. The procedure can be repeated to cover a specific range of frequencies.

4.4 Results of dynamic stability in supersonic

A total of 10 tests are conducted consecutively in the vacuum. The evolution in time of the amplitudes of the oscillating system (i.e. the angle of attack) are shown in Figure 15-left and Figure 15-right for configurations without and with flow, respectively. In both situations repeatability is excellent, and many cycles can be used for the post-processing. In the configuration with flow, however, oscillations do not damp completely.

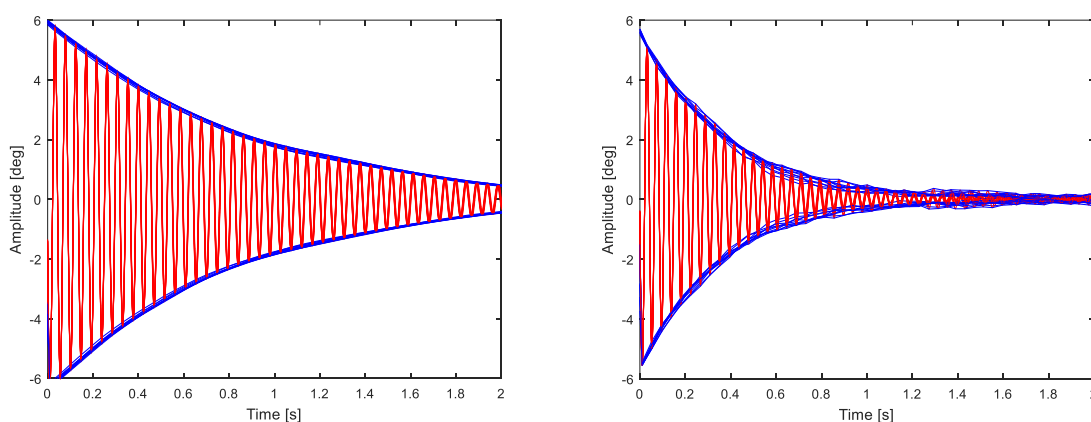


Figure 15: Oscillation and its envelope for 2 springs of 1.0mm: left - no flow; right - flow

The frequency and the damping of the dynamic system can be calculated from these measurements. In Figure 16, it can be observed that the frequency slightly increases at lower amplitudes in the configuration without flow. This is due to the lower mechanical damping seen in Figure 17-left.

Considering the stiffness of the system without flow as constant, we deduce from Eq. 5 that the inertia of the system also presents a variation with the amplitude of the oscillation, as seen in Figure 18. Indeed, it had been seen, that values of I_{yy} varies with amplitude, from 1000 kgmm^2 to 1100 kgmm^2 , which is close enough to 1040 kgmm^2 reported in Sec. 4.2.1. Since I_{yy} is not constant, the value is selected in order to have the calibration of the spring correct for higher amplitudes. It is difficult to validate this hypothesis, but fortunately the possible error made on the Inertia does not exceed 2% and the sensitivity of the result should remain small (Cm_q is proportional to the inertia).

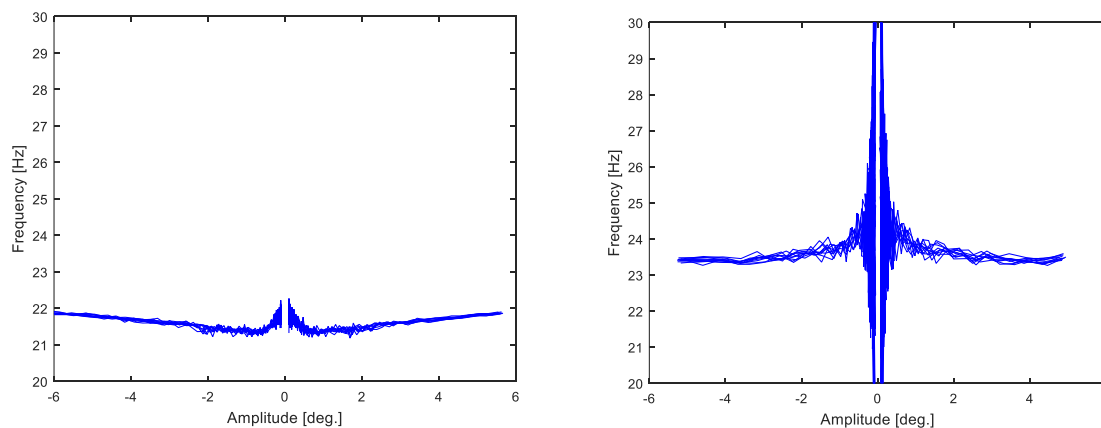


Figure 16: Frequency vs Amplitude for 2 springs of 1.0mm: left - no flow; right – Mach 0.8

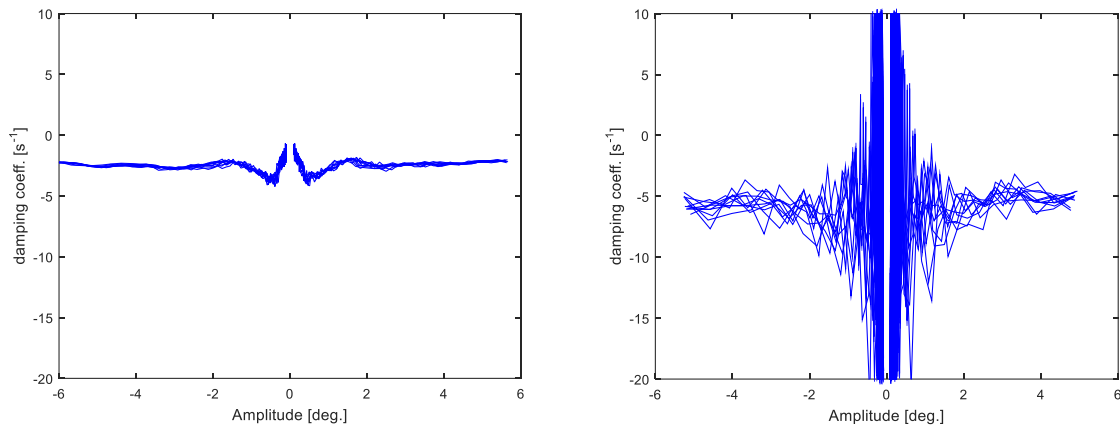


Figure 17: Damping vs Amplitude for 2 springs of 1.0mm: left - no flow; right – Mach 0.8

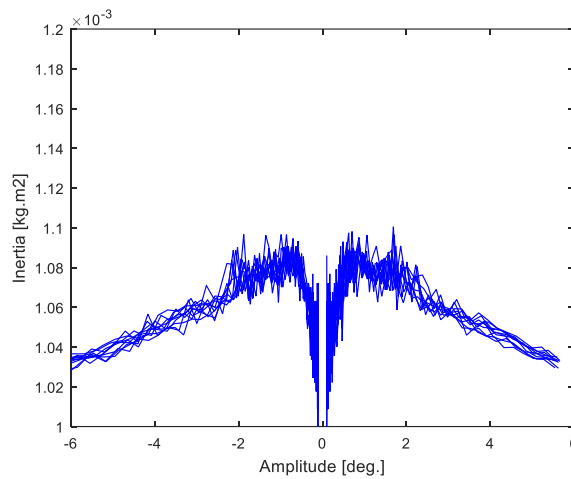


Figure 18: Inertia for 2 spring 1.0mm: no flow– Mach 0.8

Under the configuration with flow at Mach 0.8, it can be observed in Figure 16-right that frequencies are higher than those without flow, especially at lower amplitudes. This is caused by the aerodynamic stiffness added into the system. Also, the damping coefficient is significantly noisier in the presence of flow, as seen in Figure 17-right.

$$a = \frac{2}{nT} \ln \left(\frac{x_2}{x_1} \right) \quad (6)$$

T is the period of the signal

x1 and x2 are two extreme values separated by n periods

Therefore, only those amplitudes within 1.5° and 4.5° will be considered to compute the aerodynamic coefficients. The damping coefficient is calculated with the envelop method thanks to the Eq. 6. Only the amplitudes within 1.5° and 4.5° will be considered.

For illustration purposes, the total damping of the system is compared to the configurations with flow and without flow in Figure 19-left. Clearly, the mechanical damping (without flow) due to spring and ceramic bearings is less noisy than the damping with flow. Also, its magnitude is lower than the damping measured with flow. The aerodynamic damping is in the same order of magnitude as the mechanical damping, which is considered low. The aerodynamic damping coefficient $Cm_q + Cm_{\dot{\alpha}}$ is provided by the equation 7 in Figure 19-right.

$$Cm_q + Cm_{\dot{\alpha}} = - \frac{Ia}{q_{\infty} S D \frac{D}{2U_{\infty}}} \quad (7)$$

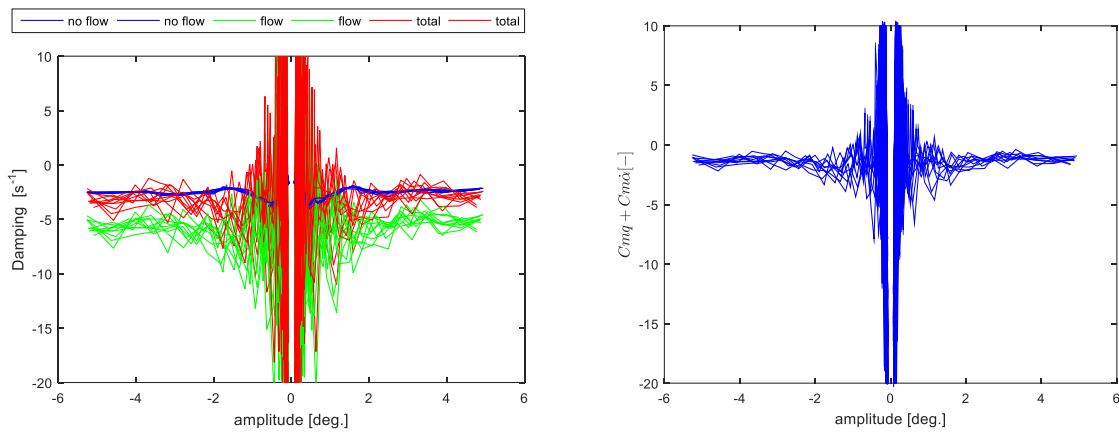


Figure 19: Damping at Mach 0.8 for 2 springs 1.0mm: left - comparison; right - Aerodynamic coefficient

Figure 20 shows the results obtained with different inertia. It can be concluded that, whatever the frequency, the value of the damping coefficient is similar and quite low. Also, since the aerodynamic damping coefficients are negative, we can conclude that the vehicle is dynamically stable.

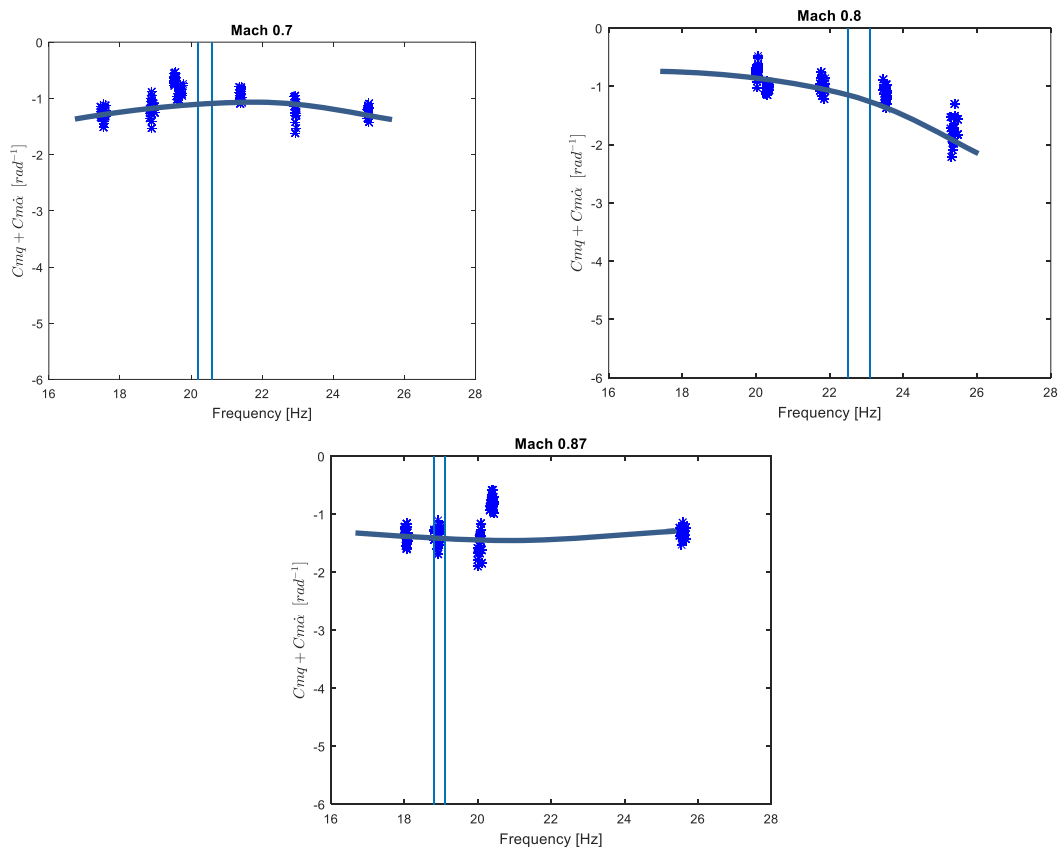


Figure 20: Damping coefficient at Mach 0.7, 0.8 and 0.9 for amplitudes [1.5-4.5]°

5 Concluding remark

The results presented above are subject to uncertainties, mostly linked to the measurement of the angle of attack, the flow characterization in the free-stream and the stiffness of the spring. All these parameters are measured with high accuracy and cannot be responsible of the discrepancy observed in Figure 20.

It is important to consider that the damping phenomena results from the delay taken by the flow to find a stable topology when the model is oscillating and in case of detachment, the separation line is moving. These phenomena are, by definition, not very repeatable because shocks are moving throughout the oscillation and the free-stream flow itself is subject to small variations. Movies taken during the test at Mach 2 with the Schlieren set up showed shock oscillations induced both by both the nozzle and by the decelerator [8] Therefore, they are the most probable reason that could explain the observed discrepancies. For these experiments in subsonic, the shocks are not yet present, and the discrepancy is much lower than for the test at Mach 2.0 [8].

6 References

- [1] B. van Hove, G. Medici, D. Bonetti, “*Preliminary Aerodynamic Database v1.0 report*”, Technical report, RRTB project, H2020 grant 870340, D6.1, DEIMOS Space, March 2021.
- [2] B. van Hove, G. Medici, D. Bonetti, “*Preliminary Aerodynamic Database v1.0 report*”, Database in mat file, RRTB project, H2020 grant 870340, D6.3 coeff_RRTB_OMLv8_V11, DEIMOS Space, March 2021.
- [3] B. van Hove, G. Medici, D. Bonetti, “*Aerodynamic Database v8*”, Power Point presentation, RRTB project, H2020 grant 870340, RRTB-CMS-SUPSC03-PRE013-11, DEIMOS Space, January 2021.
- [4] S. Paris, “*Practical aspect of the free-to-tumble technique for dynamic characterization of reentry vehicle*”, in Experimental determination of dynamic stability parameters, VKI Lecture Series, LS 2008-02, Von Karman Institute for Fluid Dynamics, Belgium, 2008.
- [5] R. Bergström, “*GNC Trilateral Update Meeting*”, Power Point presentation, RRTB project, H2020 grant 870340, Pangea_GNC_update_22092020, PANGEA Aerospace, September 2020.
- [6] D. Bonetti, R. Bunt, B. van Hove, G. Medici, “*Reference DRL Azores*”, Database in Excel sheet, RRTB project, H2020 grant 870340, RRTB-DMS-SUP-FIL0003, DEIMOS Space, March 2021.
- [7] *RRTB-CMS-SUPSC03-PRE013-11_Telecon_PA_DMS_VKI_aerodb v2.pdf*
- [8] S.Paris, A. Viladegut, F.Pinna, “*Supersonic Wind Tunnel Test and CFD Analysis Report*” Technical report, RRTB project, H2020 grant 870340, D6.5, DEIMOS Space, March 2021.
- [9] Rasmus Bergström, Nicola Palumbo, Laura Martí Ramos, Bart Van Hove, Giovanni Medici, Alan Viladegut, Sébastien Paris, Maximilian Soepper, Pranav Bhardwaj, Dimitrios Rellakis, Panagiotis Trifa, Athanasios Dafnis, Marco Kanngießner, Stefano Piacquadio, “*A novel design approach for a reusable vtol micro launch vehicle*”, IAC 2021 Congress Proceedings, 72nd International Astronautical Congress (IAC), Dubai, United Arab Emirates, 2021.
- [10] Giovanni Medici, Bart Van Hove, Rasmus Bergström, Laura Martí Ramos, “*Aerodynamic Vehicle Design, Flying Qualities, and Mission Analysis for a Reusable VTOL Micro-Launcher First Stage*”, IAC 2021 Congress Proceedings, 72nd International Astronautical Congress (IAC), Dubai, United Arab Emirates, 2021.
- [11] Dániel G. Kovács, Sebastien Paris, Guillaume Grossir and Christophe F. Schram. “*An Experimental Approach to Determine the Aerodynamic Pitch Damping Coefficient of Slender Bodies in the Transonic Regime*”, AIAA 2020-3105. AIAA AVIATION 2020 FORUM. June 2020.